Spatiotemporal Evolution of Recurrent Slow Slip Events Along the Southern Ryukyu Subduction Zone, Japan, From 2010 to 2013

doi: 10.1029/2018JB016072

Journal of Geophysical Research: Solid Earth

RESEARCH ARTICLE
10.1029/2018JB016072

Special Section:
Slow Slip Phenomena and Plate Boundary Processes

Spatiotemporal Evolution of Recurrent Slow Slip Events Along the Southern Ryukyu Subduction Zone, Japan, From 2010 to 2013

Masayuki Kano[1], Jun'ichi Fukuda[2], Shin'ichi Miyazaki[3], and Mamoru Nakamura[4]

[1]Graduate School of Science, Tohoku University, Sendai, Japan, [2]Earthquake Research Institute, The University of Tokyo, Tokyo, Japan, [3]Graduate School of Science, Kyoto University, Kyoto, Japan, [4]Faculty of Science, University of the Ryukyus, Nishihara-cho, Japan

Key Points:
- Spatiotemporal evolutions are described for five slow slip events (SSEs) with M_w 6.6–6.7 in the southern Ryukyu subduction zone
- The final slip distributions of the five SSEs are similar, indicating that the SSEs recur in the same fault area
- The temporal evolution of the five SSEs, especially the nucleation styles, varies from event to event

Supporting Information:
- Supporting Information S1

Correspondence to:
M. Kano,
masayuki.kano.a3@tohoku.ac.jp

Citation:
Kano, M., Fukuda, J.'i., Miyazaki, S.'i., & Nakamura, M. (2018). Spatiotemporal evolution of recurrent slow slip events along the southern Ryukyu subduction zone, Japan, from 2010 to 2013. *Journal of Geophysical Research: Solid Earth*, *123*, 7090–7107. https://doi.org/10.1029/2018JB016072

Received 9 MAY 2018
Accepted 23 JUL 2018
Accepted article online 31 JUL 2018
Published online 29 AUG 2018

Abstract Slow slip events (SSEs) with a moment magnitude of 6.6–6.7 occur at intervals of 5–9 months along the southern Ryukyu subduction zone in southwestern Japan. To obtain detailed image of these SSEs, this study applies a modified Network Inversion Filter to the Global Navigation Satellite System time series from March 2010 to February 2013 and estimates the spatiotemporal evolution of slow slip on the plate interface. Five SSEs are detected during this period. These events have similar cumulative slip distributions and are located near the northwestern coast of Iriomote Island at depths of 30–60 km, indicating that the SSEs recur in the same fault area. The analysis reveals that the spatiotemporal evolution of slip during the five SSEs varies from event to event. The notable feature is that three of the five SSEs nucleate rapidly and reach the maximum slip rate within several days, while the other two SSEs show much slower nucleation, lasting for 25–45 days prior to rapid acceleration of slip. Such variations in spatiotemporal evolution suggest temporal changes of fault properties such as fluid distribution and fault friction. Very low frequency earthquakes and low-frequency earthquakes are activated during one of the five SSEs. The source area of the SSEs is complimentarily located in a deeper part of the very low frequency earthquakes and low-frequency earthquake source areas, and a possible tsunami source region is located near the trench, indicating the depth dependence of the physical properties along the plate interface.

Plain Language Summary A slow slip event (SSE) is a spontaneous slow aseismic fault slip that typically occurs adjacent to the megathrust earthquake zone on plate interfaces. SSEs play an important role in plate subduction systems by modulating seismic/aseismic fault slips. However, the underlying physical mechanism of SSE generation remains unclear. This study estimates the spatiotemporal evolution of five recurrent SSEs from 2010 to 2013 along the southern Ryukyu subduction zone in southwest Japan to reveal variations in source processes of the recurrent SSEs, which may provide important insights into physical mechanisms of SSEs. Slip distributions of the five SSEs are quite similar, indicating that SSEs recur in the same fault area. In contrast, the temporal evolutions of the SSEs, especially their nucleation styles, vary with events, suggesting temporal variations of physical properties such as fluid distribution and frictional properties along the plate interface. The SSE source area is located at the deeper part of the areas where other types of slow but seismic fault slips called very low frequency earthquakes and low-frequency earthquakes occur, and a possible tsunami source region near the trench, indicating the depth dependence of physical properties along the plate boundary.

1. Introduction

Recent development of geodetic and seismic observation networks enables us to detect a new type of fault slip events in worldwide tectonic zones, categorized as slow earthquakes (Ide et al., 2007). Slow earthquakes typically occur in the transition zone between the locked seismogenic zone in shallower regions where large earthquakes nucleate and the freely slipping zone in deeper regions along the plate boundary. These earthquakes are characterized by spontaneous fault ruptures with longer durations and lower slip rate than ordinary earthquakes of the same magnitude. Slow earthquakes include slow slip events (SSEs), very low frequency earthquakes (VLFEs), low-frequency earthquakes (LFEs), and nonvolcanic low-frequency tremors (Obara & Kato, 2016; Peng & Gomberg, 2010; Schwartz & Rokosky, 2007). SSEs are slow transient fault motions that last for days to years and do not radiate seismic waves. Geodetic instruments such as the Global Navigation Satellite System (GNSS), tiltmeters, and strainmeters can help detect SSEs in many plate boundaries.

Analyses of geodetic data have clarified that a series of SSEs recurring in a specific region has a characteristic duration, recurrence interval, and magnitude, with some fluctuations depending on the region (e.g., Heki & Kataoka, 2008; Hirose & Obara, 2010; Rogers & Dragert, 2003; Szeliga et al., 2008; Yoshioka et al., 2015). These regional differences could be controlled by many factors, such as frictional properties and stress state on the fault, fluid distribution near the plate boundary, and plate geometry (e.g., Matsuzawa et al., 2010; Schmidt & Gao, 2010). However, the physical mechanism of SSE generation itself remains unclear.

Previous studies have reported that stress transfer from SSEs often modulates other seismic and aseismic slip events in the area adjacent to the SSE region, including deep low-frequency tremors (Rogers & Dragert, 2003), other SSEs (Hirose & Obara, 2005), small earthquakes (Segall et al., 2006), and possibly large magnitude (~7) earthquakes (Graham et al., 2014; Ito et al., 2013). For example, SSE propagation correlates well with the migration of tremors (Bartlow et al., 2011; Hirose & Obara, 2010; Wech & Bartlow, 2014) and small earthquakes (Fukuda et al., 2014; Hirose et al., 2014). Hirose et al. (2014) suggested that earthquake swarms are mainly driven by stress transfer from SSEs. Therefore, investigating the detailed spatiotemporal evolution of SSEs can help to quantitatively evaluate spatial and temporal effects of SSE occurrence on seismic/aseismic phenomena in adjacent fault regions and can provide important information about the physical mechanisms of SSEs.

Geodetic measurements have shown that SSEs recur at an approximately regular interval in a specific region. In the Bungo channel in southwest Japan, long- and short-term SSEs occur every ~6 years (Yoshioka et al., 2015) and ~6 months (Hirose & Obara, 2005, 2010; Sekine et al., 2010), respectively. Recurrence intervals of SSEs are ~14 months in the Cascadia subduction zone (Rogers & Dragert, 2003) and 3–4.5 years in the Guerrero region of the Mexican subduction zone (Graham et al., 2016). Whether or not these recurrent SSEs occur in the same patch on the fault with similar temporal evolution of slip is important to understand the slip style of the fault and the mechanisms governing the generation of SSEs, including the temporal change of the fault frictional properties and fluid pressure distribution. To compare and contrast recurrent SSEs, many previous studies analyzed geodetic data to estimate spatial distributions of slip of recurrent SSEs using time-independent inversion methods and showed that the location of slip is similar within each SSE series (e.g., Heki & Kataoka, 2008; Sekine et al., 2010). In contrast, Szeliga et al. (2008) found that the spatial distributions of SSEs in Cascadia varied from event to event. On the other hand, only a few time-dependent inversion analyses have compared the temporal change of slip distribution among recurrent SSEs. For example, Yoshioka et al. (2015) estimated the source process of three long-term SSEs in the Bungo channel in the Nankai subduction zone and found that the final slip distributions are nearly identical, while the propagation direction of slip differs from event to event. Fukuda (2018) imaged the spatiotemporal evolution of five SSEs off the Boso Peninsula in central Japan to show that nucleation patterns of SSEs as well as slip propagation directions and speeds vary with each event but always correlate highly with seismicity. These time-dependent analyses enable us to reveal the similarities and differences in the spatiotemporal evolution of slip within a single series of SSEs. However, our knowledge of such variability is still limited.

This study aims to image the detailed source process of recurrent SSEs beneath the Yaeyama Islands along the southern Ryukyu subduction zone in the most southwestern part of Japan (Figure 1). The plate convergence rate beneath the Yaeyama Islands is 12–13 cm/year, consisting of the subduction of the Philippine sea plate (PH) northwestward at a rate of 8.0–8.5 cm/year (Sella et al., 2002) beneath the Ryukyu Arc (Figure 1) and the southward back-arc spreading at a rate of 3.5–5.0 cm/year (Nishimura et al., 2004) along the Okinawa trough (Sibuet et al., 1998).

Along the southern Ryukyu subduction zone near the Yaeyama Islands, there are no historical records of earthquakes with a moment magnitude (M_w) greater than 8.0 during the last 300 years (Ando et al., 2009). The lack of large earthquakes is consistent with the weakly coupled subduction interface inferred from the GNSS velocity field (Nishimura et al., 2004). However, based on tsunami height records, Nakamura (2009) pointed out the possibility that a M_w 8.0 tsunami earthquake occurred in 1771 at the shallow part of the southern Ryukyu subduction zone (Figure 1). On the other hand, Goto et al. (2010) claimed that the tsunami was caused by a local earthquake accompanied by a marine landslide, and therefore, whether this earthquake occurred in the shallow plate interface or not is still debated. Recently, VLFEs and LFEs have been detected at depths shallower than 25 km along the southern Ryukyu subduction zone (Ando et al., 2012; Nakamura, 2017; Nakamura & Sunagawa, 2015). The centroid moment tensor solutions of VLFEs indicate thrust type mechanisms, suggesting that these VLFEs occur on the plate interface (Ando et al., 2012). Arai

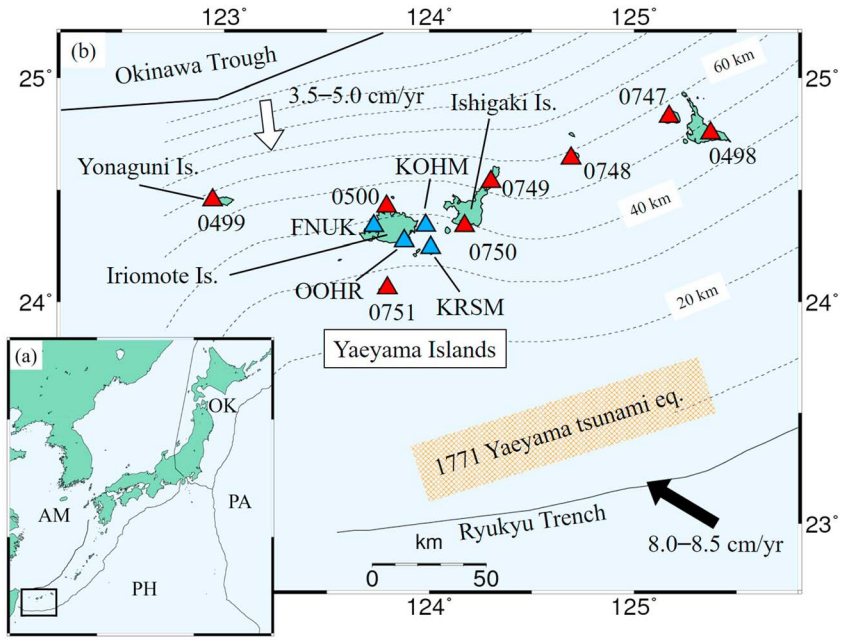

Figure 1. (a) Tectonic setting of Japan. AM, OK, PA, and PH indicate the Amurian, Okhotsk, Pacific, and Philippine Sea plates, respectively. The solid lines indicate plate boundaries. (b) A map of the Yaeyama Islands is shown by the rectangle in Figure 1a. Red and blue triangles indicate the GNSS stations operated by the Geospatial Information Authority of Japan (GSI) and Kyoto University (KU), respectively. The thick and thin lines indicate the Okinawa trough and the Ryukyu trench. The black arrow indicates the motion of the subducting PH relative to AM (Sella et al., 2002). The white arrow indicates a motion of the south Ryukyu block relative to AM, due to back-arc spreading of the Okinawa trough (Nishimura et al., 2004). The dashed lines are depth contours of the upper surface of the PH with an interval of 10 km (Hayes et al., 2012) and are extrapolated in the region off the south coast of Yonaguni Island by using the *surface* command in Generic Mapping Tools (GMT) software (Wessel & Smith, 1998). The orange region indicates the source area of the 1771 Yaeyama tsunami earthquake estimated by Nakamura (2009). GNSS = Global Navigation Satellite System.

et al. (2016) and Nakamura (2017) located the hypocenters of LFEs and showed that LFEs constitute a few clusters near the trench. In addition, Nakamura and Sunagawa (2015) investigated long-term activity of VLFEs and showed that the epicenters are complementarily located to the estimated source area of the 1771 Yaeyama earthquake (Nakamura, 2009). On the deeper part of the plate interface at depths near 30 km, SSEs with M_w~6.6 recur in an interval of 6–7 months beneath the Yaeyama Islands, with a duration of ~1 month (Heki & Kataoka, 2008; Nishimura, 2014; Tu & Heki, 2017).

Following Heki and Kataoka (2008), Tu and Heki (2017) detected 38 SSEs during 1997–2016, based on GNSS data observed at continuous stations (red triangles in Figure 1b). They estimated a simple time-independent fault model for SSEs, assuming a planar rectangular fault with spatially uniform slip. They found that SSEs exhibit a fairly regular recurrence and that the locations of slip patches are nearly identical. However, SSE magnitudes still vary, ranging from M_w 6.3 to 7.0. These SSEs, along with M_w ~7 SSEs in other regions (e.g., Ohta et al., 2006; Rousset et al., 2017; Voss et al., 2017; Wallace & Beavan, 2010), are one of the largest SSEs in the world.

This study examines the spatiotemporal source process of SSEs in the southern Ryukyu area based on a time-dependent inversion of GNSS data using a modified Network Inversion Filter (NIF; Fukuda et al., 2008). The NIF enables us to extract an accurate spatiotemporal evolution, including nucleation and propagation of slip (Fukuda, 2018; Fukuda et al., 2014). We compare and contrast the source processes of multiple SSEs. In addition, we examine the spatial and temporal correlations between SSEs and VLFEs, as well as between SSEs and LFEs, based on inferred source processes and hypocenters of the seismic events. These investigations may provide a basis for further understanding of physical properties such as frictional characteristics and fluid distributions along the plate interface, as well as interactions between SSEs and other types of slow earthquakes.

In this paper, the GNSS data analysis is described in section 2, and a brief summary of the time-dependent slip inversion scheme is presented in section 3. Spatiotemporal evolutions of SSEs are then discussed in section 4,

followed by comparisons of SSE features and the spatial and temporal relations between SSEs and other types of slow earthquakes in section 5. Finally, conclusions are presented in section 6.

2. Data Processing

In the Yaeyama Islands, eight stations (red triangles in Figure 1) from the GNSS Earth Observation Network System have been operated by the Geospatial Information Authority of Japan since 1997. However, spatial coverage is poor around Iriomote Island, where recurrent SSEs occur on the plate boundary (Heki & Kataoka, 2008). To improve the spatial and temporal resolution of slow slip, Kyoto University installed four additional GNSS stations (blue triangles in Figure 1) in this area since March 2010. We use GNSS data from the GNSS Earth Observation Network System and Kyoto University networks from 1 July 2010 to 28 February 2013. The GNSS data are processed by the GIPSY-OASIS II software (version 6.1.1), employing the precise point positioning technique (Zumberge et al., 1997) with single receiver phase ambiguity resolution (Bertiger et al., 2010). We use the final fiducial-free satellite orbit and clock products provided by the Jet Propulsion Laboratory to obtain the daily coordinates at GNSS sites. The tropospheric delays are modeled using the VMF1 mapping function (Boehm et al., 2006), and ocean tide loading is calculated using the FES2004 model (Lyard et al., 2006) and the Ocean Tide Loading Provider (http://holt.oso.chalmers.se/loading/). The estimated daily positions are transformed to the IGb08 reference frame (Rebischung et al., 2012) using the seven-parameter Helmart transformations provided by Jet Propulsion Laboratory. These transformed daily positions are used for the following data analysis.

To remove the secular trend and steps related to the antenna replacement for an individual station, we model each time series as the sum of the secular trend, steps, and displacement due to SSEs using the following equation:

$$y(t) = a + bt + \sum_i c_i H(t - T_i) + \sum_j d_j \left[1 - \exp\left(-\frac{\left(t - T_j^{\mathrm{SSE}}\right)}{\tau_j}\right)\right] H\left(t - T_j^{\mathrm{SSE}}\right) + e(t), \quad (1)$$

where $y(t)$ is the observed coordinate at time t originated from 1 July 2010, a is the initial position, b is the long-term secular velocity, $H(t)$ is a Heaviside step function, and c_i is an amplitude of ith step due to the antenna replacement at time T_i. Transient deformation due to a jth SSE is approximated by an exponential function with a time constant τ_j following Heki and Kataoka (2008) using the onset time of the SSE, T_j^{SSE}, obtained by Nakamura and Sunagawa (2015) in the fourth term on the right-hand side. Here d_j is the final displacement caused by the jth SSE. We estimate the parameters a, b, c_i, and d_j using the least squares approach and the time constant τ_j using a grid search by changing the value from 0.10 to 0.15 years (Heki & Kataoka, 2008) with an interval of 0.01 year so that the cumulative residuals, $\sum e^2(t)$, can be minimized. The estimated secular trend (second term in equation (1)) and steps (third term) are then removed from the observed data, and hereafter, we refer to this corrected time series as detrended time series, which is used for the inversion analysis. Note that the modeled SSE displacements (fourth term) are not removed. The annual and semiannual seasonal variations are not modeled because the recurrence intervals of the SSEs of about 6–7 months are similar to the periodicity of seasonal variations. We find that this simplification does not affect the inversion results in section 4. For example, the detrended time series (Figure 2) show a clear 1 to 2-cm eastward movement during the middle of 2010 and early 2011 at stations 0500, 0750, OOHR, KOHM, and KRSM. These apparent signals are found at stations on and near Iriomote Island, suggesting that transient slip occurred beneath the island. We ignored 17–20 September 2010 at all stations and 11 October 2010 to 31 May 2011 at KOHM, because of unstable observations due to a typhoon and some ambiguous effects.

3. Time-Dependent Inversion

Here we generate a model of the geometry of the upper surface of the subducting PH using depth contours of the subduction interface given by Hayes et al. (2012). The model region extends from 122.75°E to 124.5°E and from 20 to 80 km depth (Figure 3). The curved plate interface is subdivided into Delaunay triangular dislocation elements. Subsequently, the detrended time series are inverted to infer the daily temporal evolution of slip on the modeled plate interface using the modified NIF.

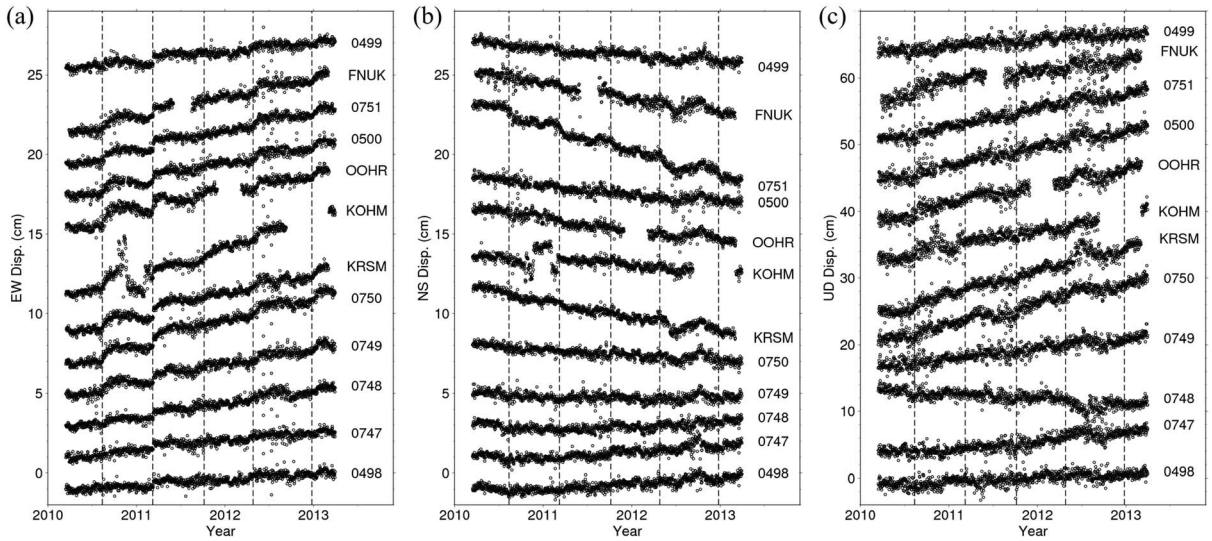

Figure 2. Detrended GNSS time series from 2010 to 2013 in (a) east-west, (b) north-south, and (c) up-down components. Each time series is sorted from the westernmost (top) to easternmost (bottom) station. The dashed lines correspond to the onsets of SSEs determined by Nakamura and Sunagawa (2015). GNSS = Global Navigation Satellite System; SSEs = slow slip events.

We provide a brief summary of the modified NIF here (see Fukuda et al. (2008) for a detailed explanation). The observation equation employed in the modified NIF is given in the following form:

$$u_n(\mathbf{x},t) = \sum_{\xi} G_n(\mathbf{x},\xi)s(\xi,t) + L_n(\mathbf{x},\mathrm{t}) + f_n(t) + \varepsilon_n(\mathbf{x},t), \quad (2)$$

where $u_n(\mathbf{x},t)$ is the nth component of the detrended time series at a station location $\mathbf{x}$ and time t. The first term on the right-hand side in equation (2) represents the displacement due to fault slip; $s(\xi,t)$ is the slip in a triangular fault at ξ; $G_n(\mathbf{x},\xi)$ represents the elastostatic Greens' function that provides the nth component of the displacement at $\mathbf{x}$ due to a unit slip at ξ and is computed assuming a homogeneous elastic half space (Thomas, 1993). The slip direction is assumed to be parallel to the plate convergence between the subducting PH and overriding Amurian Plate (Sella et al., 2002). The second term, $L_n(\mathbf{x},t)$, represents temporally correlated nontectonic local benchmark motions (Langbein & Johnson, 1997; Mao et al., 1999; Segall & Matthews, 1997). The third term, $f_n(t)$, represents spatially uniform common mode errors related to errors in the reference frame and satellite orbits (e.g., Miyazaki et al., 2003; Wdowinski et al., 1997), and the last term, $\varepsilon_n(\mathbf{x},t)$, represents random observation errors. Equation (2) represents observed displacement as the sum of displacements due to slip on the fault, temporally correlated local motions, spatially uniform errors, and random observation errors. In the modified NIF, slip distributions, $s(\xi,t)$, are represented by the superposition of spatial basis functions $b_m(\xi)$ as $s(\xi,t) = \sum_{m=1}^{N_b} b_m(\xi)c_m(t)$, where N_b is the number of basis functions that controls the spatial roughness of slip (Fukuda et al., 2008) and $c_m(t)$ is the coefficient of mth basis function $b_m(\xi)$. The number of basis functions, m, is determined to be 6 in this study by maximizing the marginal likelihood function (Fukuda et al., 2008). The modified NIF considers these coefficients, $c_m(t)$, and their time derivatives, $\dot{c}_m(t)$, as state variables to be estimated in addition to local benchmark motions, $L_n(\mathbf{x},t)$, and common mode errors $f_n(t)$.

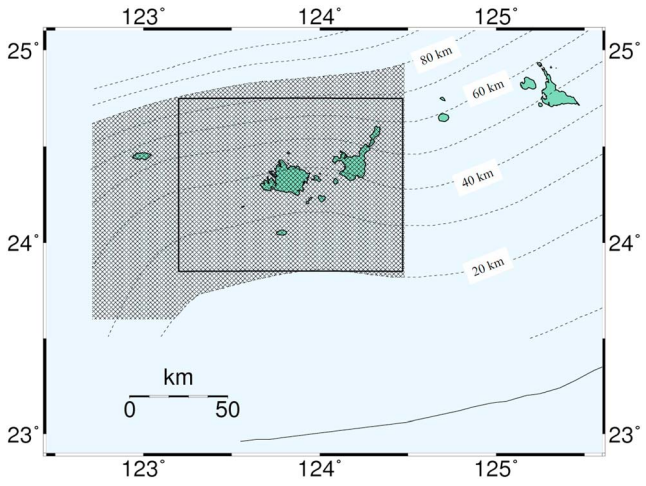

Figure 3. The modeled fault region (shaded), extending from 122.75 to 124.5°E and 20 to 80 km depth. The dashed lines indicate depth contours for the upper surface of the PH at 10-km intervals (Hayes et al., 2012) and are extrapolated in the region off the south coast of Yonaguni Island using the *surface* command in the GMT software (Wessel & Smith, 1998). Moment rate functions and seismic moments shown in Figures 4, 9, and Table 1 are calculated using the slip rate within the black rectangle. GMT = Generic Mapping Tools.

The temporal evolution of fault slip is formulated in the following discretized equations, assuming that slip rate follows a random walk process:

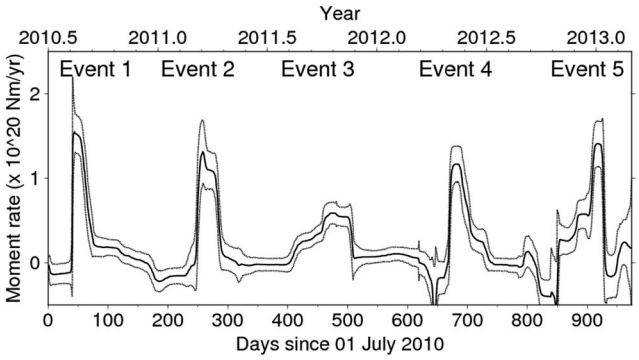

Figure 4. Temporal evolution of the estimated moment rate (solid line) within the area shown by the black rectangle in Figure 3 with 1-σ uncertainty (broken lines).

$$\begin{bmatrix} s(\xi,t_k) \\ \dot{s}(\xi,t_k) \end{bmatrix} = \begin{bmatrix} 1 & \Delta t \\ 0 & 1 \end{bmatrix} \begin{bmatrix} s(\xi,t_{k-1}) \\ \dot{s}(\xi,t_{k-1}) \end{bmatrix} + \mathbf{v}_k^{(m)}, \quad \mathbf{v}_k^{(m)} \sim N\left(\begin{bmatrix} 0 \\ 0 \end{bmatrix}, \alpha_k^2 \begin{bmatrix} \Delta t^3/3 & \Delta t^2/2 \\ \Delta t^2/2 & \Delta t \end{bmatrix} \right), \quad (3)$$

where t_k represents the kth observation epoch and Δt is the time interval of observations defined as $t_k - t_{k-1}$, which is equal to 1 day in the present study (Fukuda, 2018). Equation (3) shows that temporal roughness of slip rate is controlled by the hyperparameter α_k^2. For example, if α_k^2 is zero, the system noise $\mathbf{v}_k^{(m)}$ is zero, yielding to $\dot{s}(\xi,t_k) = \dot{s}(\xi,t_{k-1})$. This indicates that slip rate does not vary between t_{k-1} and t_k. On the other hand, if α_k^2 is large, the system noise $\mathbf{v}_k^{(m)}$ can become large, and equation (3) indicates that slip rate can vary rapidly between t_{k-1} and t_k. The standard NIF (McGuire & Segal, 2003; Segall & Matthews, 1997) assumes α_k^2 is time invariant. This assumption often leads to temporal smoothing of rapid changes in slip rate and/or excessively noisy estimates of slow temporal evolution of slip rate (Fukuda et al., 2004, 2008). For example, Bartlow et al. (2011) showed that the standard NIF estimates an amount of artificial slip before the true onset of SSEs in the Cascadia subduction zone. The primary advantage in the modified NIF is that α_k^2 is modified to vary temporally and stochastically. Therefore, the modified NIF can extract slip signals without significant oversmoothing or undersmoothing (Fukuda et al., 2004, 2008), and is thus able to detect small changes in slip rate, as for the onset and early acceleration phase of the 2013–2014 Boso SSE (Fukuda et al., 2014). We model the local benchmark motion as a random walk process with a scale parameter of 1 mm/year$^{1/2}$, and common mode errors are modeled as a Gaussian white noise process with a standard deviation of 20 mm. By combining the observation equation and the equations that describe the temporal evolution of state variables, the modified NIF sequentially estimates slip and slip rate on the fault, local benchmark motions, and common mode errors every day from 1 July 2010 to 28 February 2013 so that the predicted displacements are adjusted to match the observations at each day.

4. Results

4.1. Moment Rate Functions

Figure 4 shows moment rate functions calculated from the estimated daily slip rate distribution with a shear modulus of 30 GPa. The temporal evolution of moment rate shows that five significant events whose moment rate exceeds 1-σ uncertainty are detected between July 2010 and February 2013. The SSEs started approximately in 2010.6, 2011.2, 2011.6, 2012.3, and 2012.8, with a recurrence interval of 5–9 months. Hereafter, we refer to these five SSEs as Events 1–5, respectively.

4.2. Observed Features of Surface Displacements

Figures 5 and S1 show observed GNSS time series for Events 1–5. The time series are obtained by subtracting common mode errors (the third term on the right-hand side in equation (1)) from the detrended time series (Figure 2). Transient signals can be detected for all five events at stations located on and near Iriomote Island (0500, 0750, 0751, FNUK, KOHM, KRSM, and OOHR; see Figure 1 for GNSS stations). For example, the station 0500 shows rapid transient displacements of 0.6–0.9 cm to the east, 0.3–0.5 cm to the north, and 1–2 cm upward over 1.0–1.5 months during each of the five SSEs (Figure 5). Based on the observed time series, we calculate total cumulative displacement vectors for each event (Figure 6) by taking the difference between coordinates averaged over 10 days before and after the event. Figure 6a indicates that in Event 1, stations on and near Iriomote Island exhibit east-southeastward movement of 0.6–1.0 cm, which are roughly the opposite direction of horizontal movement due to the subduction of the PH, and uplifts of 0.7–1.5 cm. The spatial patterns of the total displacement vectors for Events 2–5 are similar to those for Event 1 (Figure 6), suggesting that the spatial patterns of the total slip distribution for Events 1–5 are similar.

4.3. Cumulative Slip Distributions

Cumulative slip distributions of the five events (Figure 7) indicate that SSEs occur in the same area of the fault located near the northwestern part of Iriomote Island at depths of 30–60 km, although the sparse distribution

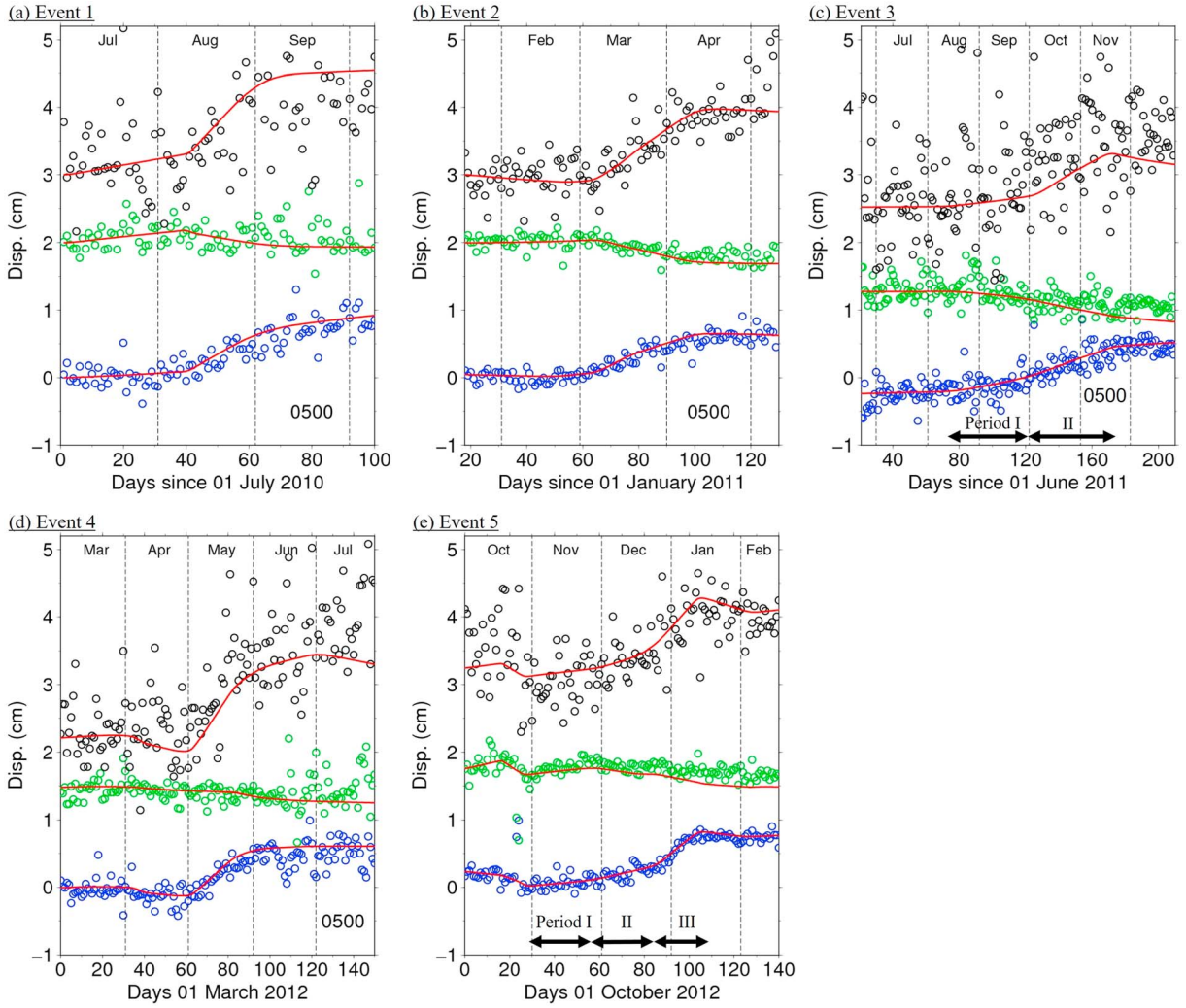

Figure 5. Observed GNSS time series (circles) at station 0500 (Iriomote) obtained by subtracting common mode errors from the detrended time series (Figure 2), with the calculated displacement (red lines) due only to slip on the plate interface for Events (a) 1, (b) 2, (c) 3, (d) 4, and (e) 5. Blue, green, and black circles indicate the east-west, north-south, and up-down components, respectively. See Figure 1 for GNSS station location. GNSS = Global Navigation Satellite System.

of the GNSS stations (Figure 1) makes it difficult to discuss the spatial distribution of SSEs in detail. The locations of the main slip regions for the five events are consistent with previously estimated locations of recurrent SSEs including these five events (Heki & Kataoka, 2008; Nishimura, 2014; Tu & Heki, 2017). The amount of maximum slip ranges from 7.0 to 9.0 cm.

4.4. Spatiotemporal Evolution of Fault Slip

Figures 8–10 show the temporal evolution of moment rate, slip rate distribution, and slip rate at a point within the large slip area (point A in Figure 7) for the five SSEs. Since there is only one station on Yonaguni Island (Figure 1), slip resolution is low beneath the island. Moreover, it would be difficult to separate slow slip signals from local benchmark motions using only one GNSS station. Therefore, we do not discuss slip near Yonaguni Island, although a small amount ($<$ 0.4 m/year) of slip can be inferred beneath Yonaguni Island prior to the onset of Events 1 and 2 (Figures 9a and 9b), in the end of Event 3 (Figure 9c), and during the initial stage of Event 5 (Figure 9e).

4.4.1. Event 1 (August–September 2010)

Figures 8a, 9a, and 10a indicate that the fault slip for Event 1 starts to accelerate rapidly with a clear onset date of 10 August 2010 near the northwestern coast of Iriomote Island, reaching a maximum slip rate of ~1.2 m/year. This rapid acceleration to the maximum slip rate occurs within a day (Figures 8a, 9a, and 10a), and slip

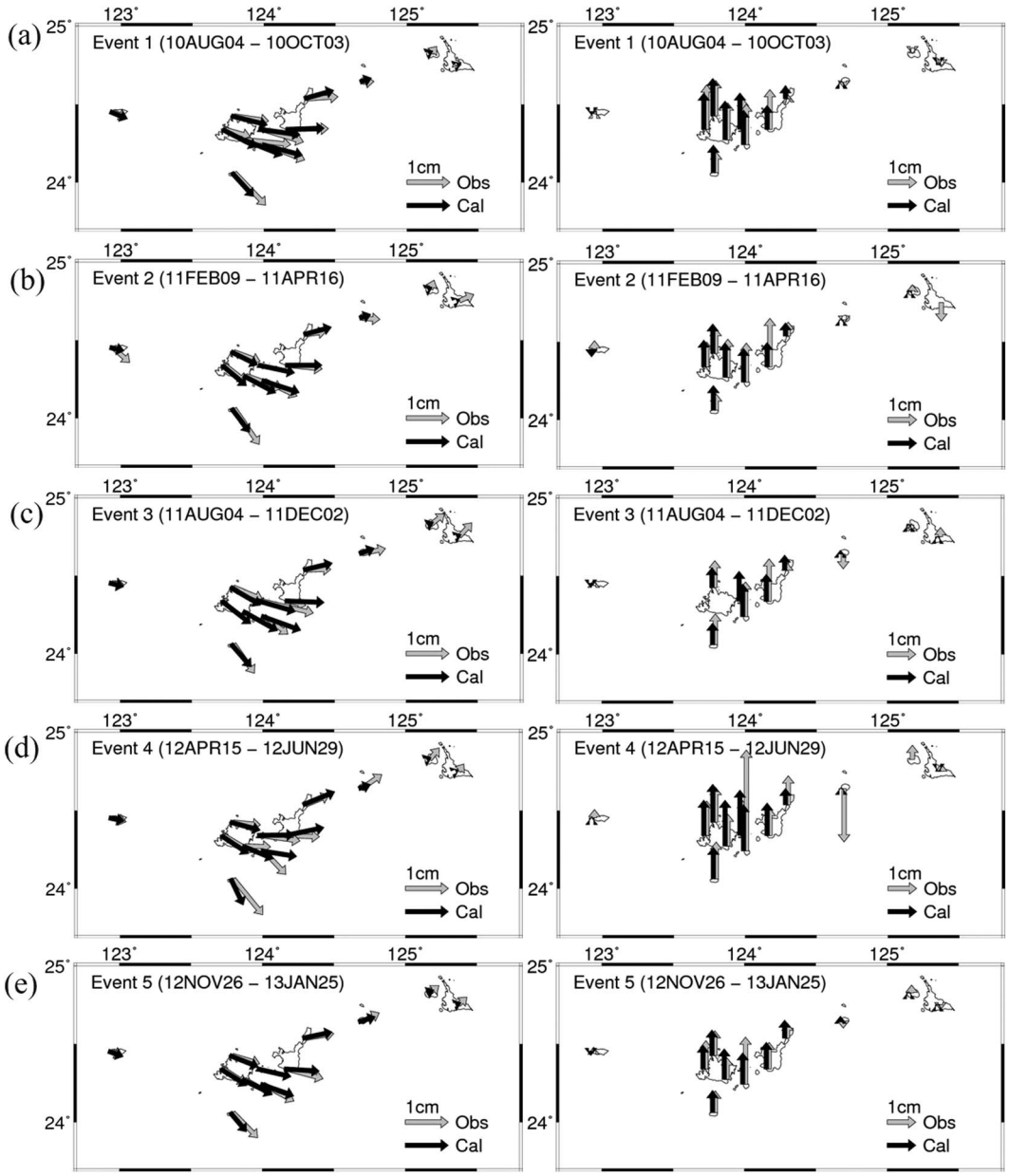

Figure 6. Observed (left) horizontal and (right) vertical GNSS displacement vectors (black arrows) with calculated ones due to fault slip (gray arrows) for Events (a) 1, (b) 2, (c) 3, (d) 4, and (e) 5. These vectors are obtained by taking the difference between coordinates averaged over 10 days before and after the event period shown in each panel. The observed displacements are corrected for secular trend, steps, and common mode errors. GNSS = Global Navigation Satellite System.

greater than 1.0 m/year continues for ~15 days in the same fault area until 22–26 August (Figure 9a). Subsequently, slip begins to decay gradually, and the slip rate at the main slip region becomes less than the 1-σ uncertainty level on 8 September (Figure 10a), although the small amount of slip (~ 0.1 m/year) slightly above the 1-σ uncertainty level continues beneath the southeast part of Iriomote Island until 20 October. The total duration of Event 1 is ~30 days, and the location of the main slip area does not vary throughout the event.

Figures 5a and S1a compare the observed time series corrected for common mode errors with calculated ones that contain contributions only due to fault slip (the first term on the right-hand side in equation (1)), indicating that the calculated time series are good fits with respect to the observed ones. In addition,

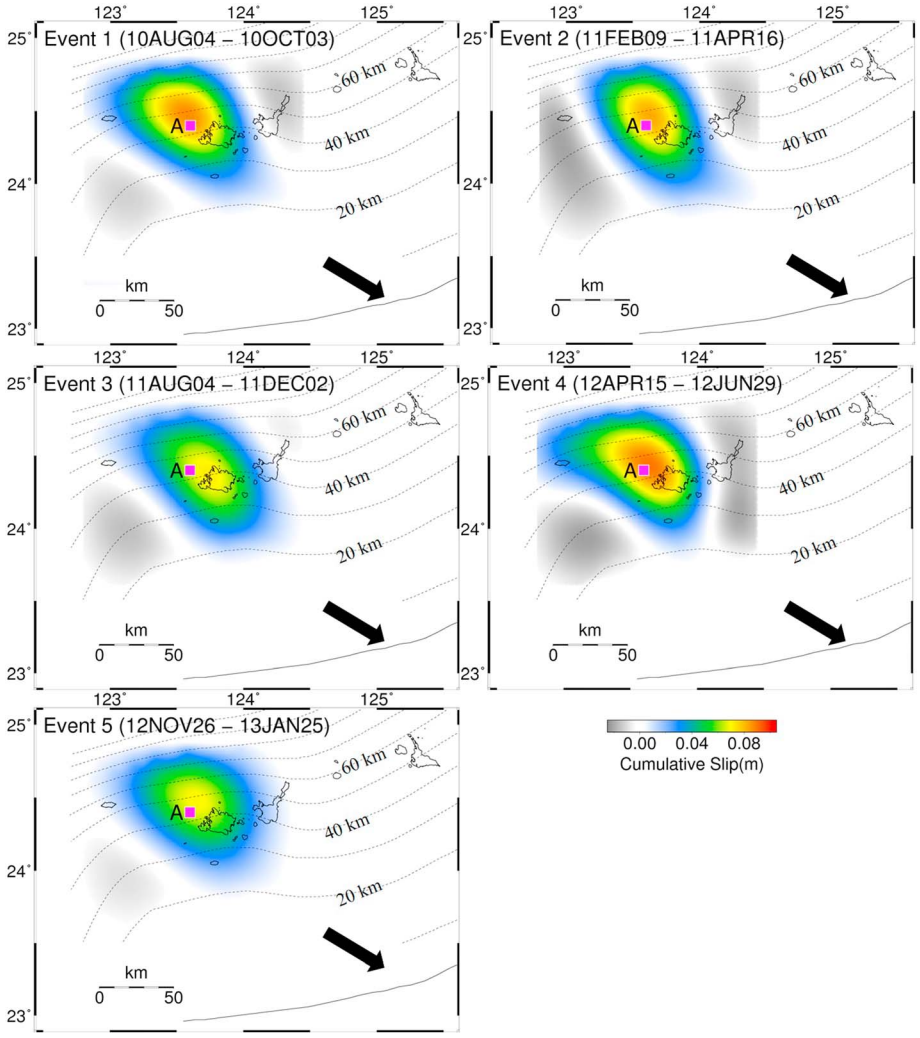

Figure 7. Cumulative slip distribution of the five SSEs during the period shown in each panel. Slip rate histories at point A are shown in Figure 10. The black line indicates the Ryukyu trench. The dashed lines are depth contours of the upper surface of the PH with an interval of 10 km (Hayes et al., 2012) and are extrapolated in the region off the south coast of Yonaguni Island by using the *surface* command in GMT software (Wessel & Smith, 1998). The black arrows indicate the positive slip direction. GMT = Generic Mapping Tools; SSEs = slow slip events.

the total displacement vectors obtained from the calculated time series match well with observed displacements (Figure 6a).

4.4.2. Event 2 (March–April 2011)

Event 2 starts around 6 March 2011 near the northwestern coast of Iriomote Island, and the fault slip reaches a maximum slip rate of 0.9 m/year around 14–18 March (Figures 8b, 9b, and 10b). It takes several days for Event 2 to reach the maximum slip rate, which is a little longer than in Event 1. However, uncertainties in the estimated slip and moment rates indicate that there is no significant difference in the slip acceleration style between Events 1 and 2. Fault slip subsequently lasts for ~30 days with a slip rate of ~0.8 m/year until early April. After that, slip gradually decelerates and stops in mid-April. The main slip area does not migrate during Event 2 (Figure 9b), and the total duration is ~35 days. Figures 5b and S1b compare the calculated time series with the observed ones and indicate a good match. Consequently, the calculated displacement vectors during Event 2 fit the observed ones well (Figure 6b).

4.4.3. Event 3 (August–November 2011)

Figures 8c, 9c, and 10c indicate that Event 3 exhibits different behavior compared with Events 1 and 2 and is characterized by slower acceleration, longer total duration, and a smaller maximum moment rate (Figures 8f

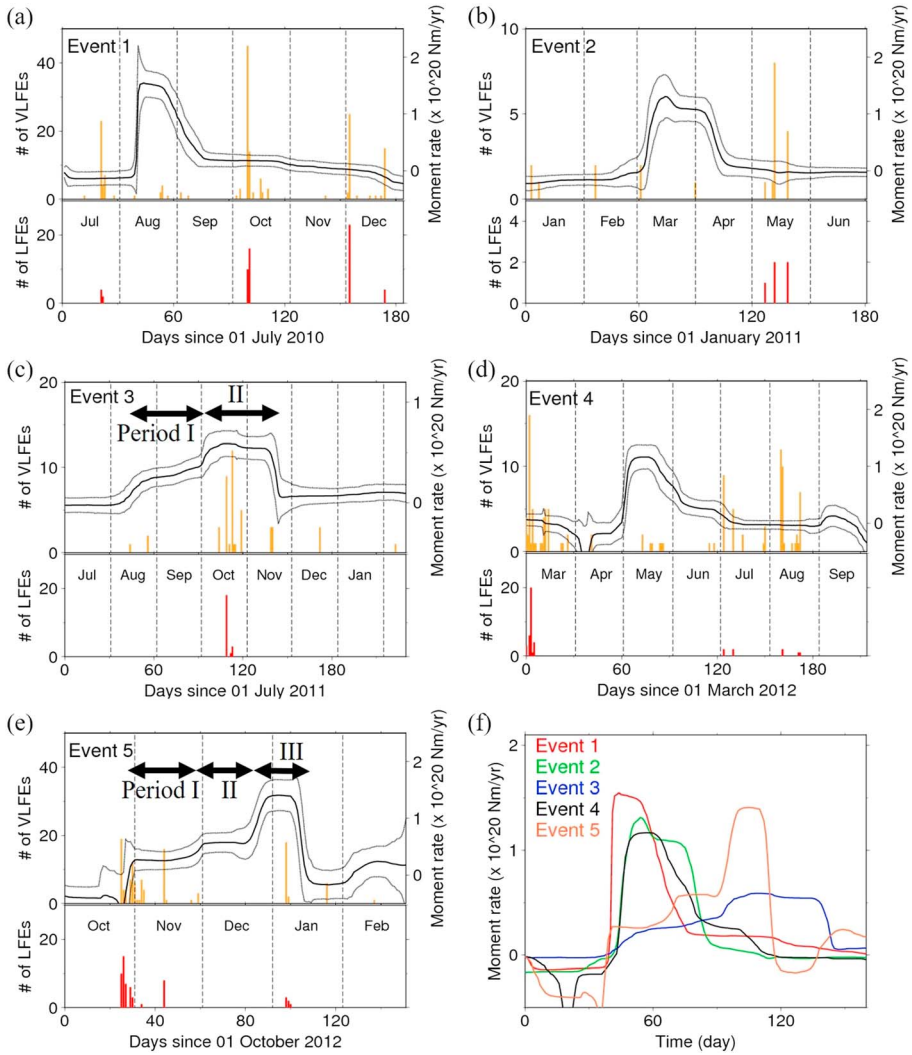

Figure 8. Time histories of moment rate (solid lines) within the area shown by the black rectangle in Figure 3 with 1-σ uncertainty (dotted lines) for Events (a) 1, (b) 2, (c) 3, (d) 4, and (e) 5. The orange and red bars indicate the numbers of VLFEs (Nakamura & Sunagawa, 2015) and LFEs (Nakamura, 2017) per day, respectively. (f) Red, green, blue, black, and orange lines indicate the moment rate functions for Events 1–5, respectively. VLFEs = very low frequency earthquakes; LFEs = low-frequency earthquakes.

and 10f). This event can be divided into two periods: Period I (mid-August to September) is characterized by a slower acceleration and subsequent slower slip rate, while Period II (October to late November) exhibits a sudden slip acceleration and a relatively faster slip rate. Figures 8c, 9c, and 10c indicate that during Period I, Event 3 initiates in mid-August 2011 near the northwestern coast of Iriomote Island, and slip accelerates slowly up to a slip velocity of ~0.15 m/year for about 1.5 months through the end of September 2011. During Period II, acceleration of slip increases suddenly in early October and slip rate reaches its maximum of ~0.4 m/year around 6 October. The maximum slip rate is 2–3 times less than that for Events 1 and 2 and lasts until the middle of November. Finally, slip shows a rapid deceleration and slip rate becomes less than the 1-σ uncertainty level during the end of November. The temporal evolution of slip rate distributions (Figure 9c) indicates that the locations of large slip area are the same for Periods I and II. The total duration of Event 3 is ~95 days, which consists of the first slow acceleration for ~45 days (Period I) and the subsequent faster slip for ~50 days (Period II).

The slow acceleration during Period I is visible in the GNSS time series (Figures 5c and S1c), which show very slow east-southeastward movements from the middle of August until the start of the significant

Figure 9. Spatiotemporal evolution of slip rate for Events (a) 1, (b) 2, (c) 3, (d) 4, and (e) 5. The orange and red dots indicate the epicenters of VLFEs (Nakamura & Sunagawa, 2015) and LFEs (Nakamura, 2017) that occurred on each day, respectively. The black line indicates the Ryukyu trench. The dashed lines are depth contours of the upper surface of the PH with an interval of 10 km (Hayes et al., 2012) and are extrapolated in the region off the south coast of Yonaguni Island by using the *surface* command in GMT software (Wessel & Smith, 1998). Note that although the slip rate is estimated every day, the slip rate distribution for each event is shown with an unequal time interval, and the color scales for Events 3 and 5 are different from other events. VLFEs = very low frequency earthquakes; LFEs = low-frequency earthquakes; GMT = Generic Mapping Tools; PH = Philippine Sea plates.

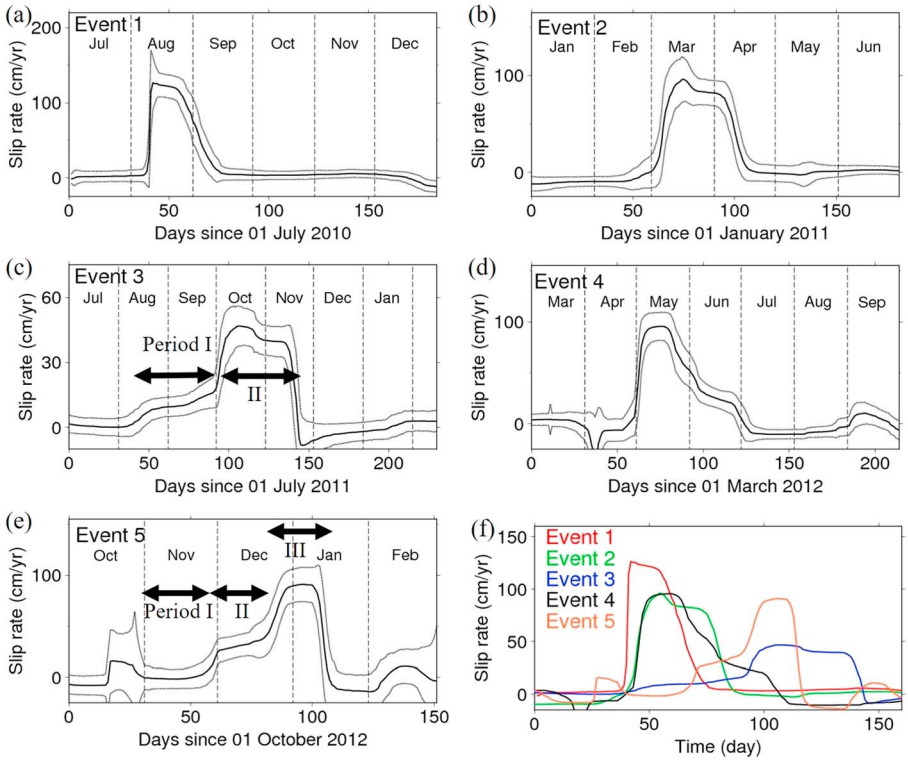

Figure 10. Time histories of slip rate (solid lines) with 1-σ uncertainty (broken lines) for Events (a) 1, (b) 2, (c) 3, (d) 4, and (e) 5, at point A in Figure 5 where large amounts of slip are estimated for all events. (f) Red, green, blue, black, and orange lines indicate time histories of slip rate at point A for Events 1–5, respectively.

east-southeastward signals in early October. Figures 11a and 11b show horizontal displacement vectors for 40 days prior to the onset of Event 3 and during Period I, respectively. These vectors are calculated by taking the difference between the mean coordinates, averaged over 5 days before and after the period shown in each panel. Before the onset of Event 3, no systematic displacements are observed (Figure 11a). In contrast, east-southeastward movements of 1–3 mm are observed during Period I (Figure 11b). The spatial pattern of the displacement vectors is analogous to the total displacement (Figure 6c), suggesting that these east-southeastward movements are caused by slow fault slip. Nakamura and Sunagawa (2015) examined the onset of SSEs by fitting the exponential function in equation (1) to the GNSS data and determined the onset of Event 3 to be 6 October 2011. This onset time is significantly different from ours (mid-August 2011) but is consistent with our initiation time for Period II. The different onset times of Event 3 result from the fact that the exponential function is not capable of capturing the gradual acceleration of the slip during Period I; consequently, Nakamura and Sunagawa (2015) detected only the faster slip during Period II. In contrast, since the modified NIF does not assume any deterministic function for fault slip evolution (see equation (3)), we successfully identify the slow slip acceleration during Period I as well as the faster slip during Period II.

4.4.4. Event 4 (April–June 2012)

Event 4 starts around 30 April 2012 near the northwestern coast of Iriomote Island, and slip rapidly accelerates within a few days to reach a maximum slip rate of ~1.0 m/year in early May (Figures 8d, 9d, and 10d). The maximum slip rate continues for ~15 days until 17 May, followed by a gradual decay through the end of June. No significant propagation of slip is found during Event 4, and the total duration is ~60 days. The displacement time series at the GNSS observation sites reproduce the observed ones well (Figures 5d and S1d). The temporal evolutions of moment rate (Figure 8d) and slip rate at the large slip area (Figure 10d) show that this event is characterized by the rapid nucleation of slip, similar to the temporal evolution of Events 1 and 2 (Figures 8f and 10f). This indicates that Event 4 is a recurrence of Events 1 and 2.

4.4.5. Event 5 (November 2012–January 2013)

The temporal evolution of moment rate (Figure 8e) and slip rate distributions (Figure 9e) indicates that Event 5 can be divided into three periods, each of which has different characteristics of spatiotemporal slip

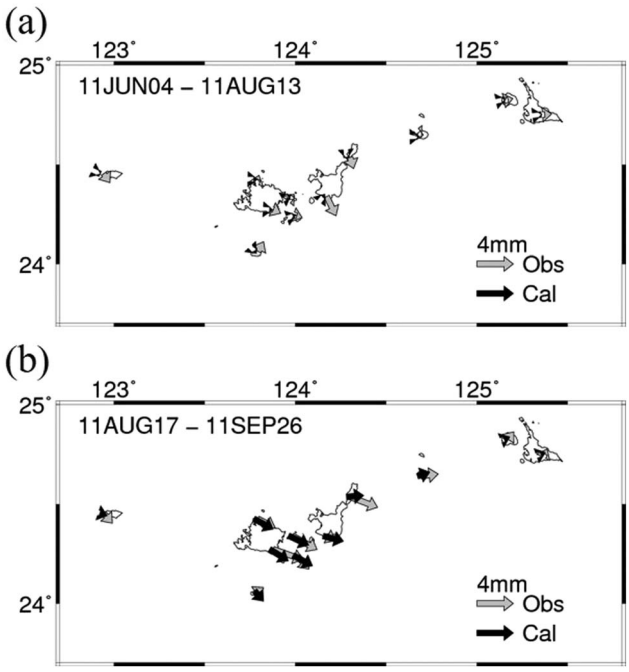

Figure 11. Observed (black arrows) and calculated (white arrows) displacement vectors for 40 days (a) before the onset of Event 3 and (b) during Period I of Event 3. These vectors are obtained by taking the difference of mean coordinates averaged over 5 days before and after the period shown in each panel. The observed displacement vectors are corrected for secular trend, steps, and common mode errors, and the calculated ones represent displacements due only to fault slip.

evolution: a slow fault slip beneath the northern coast of Ishigaki Island from late October to late November (Period I), a slow slip acceleration beneath the northwestern coast of Iriomote Island from late November to late December (Period II), and a more rapid acceleration of slip and the subsequent faster slip rate until the middle of January (Period III). The moment rate shows negative values just before the onset of Event 5 (the first half of October 2012) due to some ambiguous negative slip beneath the south part of Ishigaki Island, but this negative slip is not discussed. In Period I, slip accelerates and the moment rate exceeds 1-σ uncertainty at the end of October (Figure 8e) beneath the northern coast of Ishigaki Island (Figure 9e), where no significant slip was estimated for Events 1–4. The slip near Ishigaki Island continues with a rate of ~0.25 m/year for ~30 days and ceases around 27 November. During Period II, slip begins to accelerate at the end of November beneath the northwestern coast of Iriomote Island, where large amounts of slip have been estimated for Events 1–4, and continues to accelerate gradually for the following 25 days (Figure 10e). Finally, in Period III, slip starts to accelerate rapidly on ~21 December and reaches a maximum slip rate of ~0.9 m/year by the end of the month (Figures 9e and 10e). The maximum slip rate lasts for ~10 days and finally begins to decelerate around 10 January, terminating a few days later. This temporal evolution characterized by slower acceleration during Period II and a rapid reacceleration in Period III is similar to Event 3. The observed GNSS time series show slower transient signals during Periods I and II, followed by rapid signals during Period III (Figures 5e and S1e). These observations are explained well by the estimated slip evolution in Figures 5e and S1e.

5. Discussion

5.1. Characteristics of Recurrent SSEs in the Southern Ryukyu Region

We have detected five SSEs during the period from July 2010 to February 2013 in the southern Ryukyu region. These five SSEs occur beneath the northwestern coast of Iriomote Island at depths of 30–60 km with quite similar cumulative slip distributions (Figure 7) and have nearly the same seismic moments of $1.0–1.2 \times 10^{19}$ Nm, which are equivalent to M_w of ~6.6–6.7 (Table 1). These results indicate that the SSEs recur in the same patch on the fault.

In contrast to the similarity in final slip distributions, we found that the spatiotemporal evolution of the five SSEs is significantly different for each event (Figures 8–10). In terms of SSE nucleation, the five SSEs are categorized into two groups: Events 1, 2, and 4 (Group 1), and Events 3 and 5 (Group 2). The SSEs in Group 1 show sudden acceleration from zero to the maximum slip rate within several days (Figure 10f). On the other hand,

Table 1
Cumulative Moment, Moment Magnitude (M_w), Duration and Maximum Slip Rate for the Five SSEs

	Cumulative moment (Nm)	M_w	Duration (days)	Maximum slip rate (m/year)
Event 1	$1.1 \pm 0.2 \times 10^{19}$	6.6	~30	1.2 ± 0.2
Event 2	$1.1 \pm 0.3 \times 10^{19}$	6.6	~35	0.8 ± 0.1
Event 3	$1.1 \pm 0.3 \times 10^{19}$	6.6	~45 (Period I) ~50 (Period II)	0.4 ± 0.1
Event 4	$1.2 \pm 0.3 \times 10^{19}$	6.7	~60	1.0 ± 0.1
Event 5	$1.1 \pm 0.4 \times 10^{19}$	6.6	~30 (Period I) ~25 (Period II) ~25 (Period III)	0.9 ± 0.1

Note. The cumulative moment is calculated using only the positive slip rate within the area outlined by the black rectangle in Figure 3.

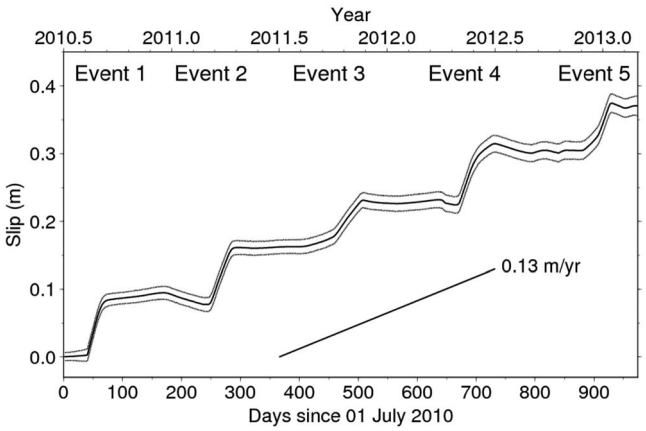

Figure 12. Temporal evolution of the estimated slip (solid line) at the main slip area (point A in Figure 7) with 1-σ uncertainty (broken lines).

the SSEs in Group 2 exhibit much more gradual nucleation for ~25–45 days, followed by rapid acceleration to the maximum slip rate. This rapid acceleration is comparable to that for the events in Group 1. However, the maximum slip rate and duration are not systematically different between the two groups. The maximum slip rate for most of the SSEs is similar (~0.8–1.2 m/year), with an exception of ~0.4 m/year for Event 3 (Table 1 and Figure 10f). Similarly, Events 1, 2, 4, and 5 exhibit similar durations of maximum slip rate (~20–30 days), while Event 3 duration is significantly longer (~50 days, Figure 10f). Overall, total duration varies from 30 to 95 days, reflecting differences in SSE nucleation and deceleration styles (Table 1).

Similar variations in nucleation style within a single series of SSEs are also found in the SSEs off the Boso Peninsula in central Japan (Fukuda, 2018). Another similarity for the SSEs in both regions is that the maximum slip rate durations are comparable. SSEs in the Boso area exhibit a correlation between nucleation style and the maximum slip rate/seismic moment; events with rapid nucleation have a faster maximum slip rate and larger seismic moment than events with slower nucleation (Fukuda, 2018). The maximum slip rate for Event 3 in the Ryukyu area, which exhibits slower nucleation, is smaller than those for Events 1, 2, and 4, suggesting a correlation between nucleation style and maximum slip rate similar to that for the Boso SSEs. However, Event 5 has a maximum slip rate that is more comparable to Events 1, 2, and 4. Therefore, it is not clear whether the correlation found in the Boso area is applicable to the SSEs in the southern Ryukyu area.

In summary, SSEs in the southern Ryukyu area rupture the same fault patch, but the temporal evolution of slip, especially the nucleation style, differs from event to event. However, the spatial resolution of slip is low due to the limited number of stations (Figure 1). Installation of additional stations will more clearly reveal similarities and differences among SSEs in the southern Ryukyu area, enabling further comparisons between SSEs in the southern Ryukyu area and those in other subduction zones.

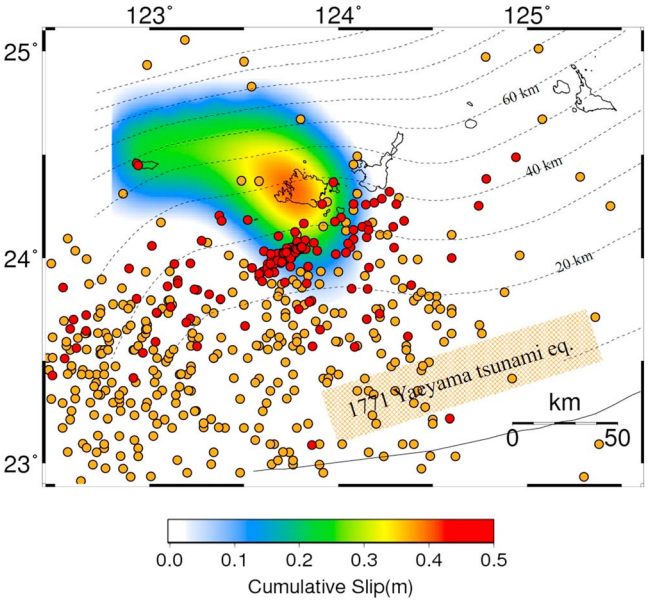

Figure 13. Cumulative slip distribution from July 2010 to February 2013, compared with the epicenters of VLFEs (orange dots, Nakamura & Sunagawa, 2015) and LFEs (red dots, Nakamura, 2017). The thin and dashed lines are the Ryukyu trench and the depth contours of the upper surface of the PH with an interval of 10 km (Hayes et al., 2012) and are extrapolated in the region off the south coast of Yonaguni Island by using the *surface* command in GMT software (Wessel & Smith, 1998). The orange region is the source area of the 1771 Yaeyama tsunami earthquake (Nakamura, 2009). VLFEs = very low frequency earthquakes; LFEs = low-frequency earthquakes; GMT = Generic Mapping Tools; PH = Philippine Sea plates.

Figure 12 shows the cumulative slip in the main slip area of the SSEs (point A in Figure 7), indicating that the slip rate averaged over the entire analysis period is ~0.13 m/year. This average slip rate is comparable to the plate convergence rate of ~0.13 m/year in the southern Ryukyu subduction zone, consisting of the PH subduction rate of 0.080–0.085 m/year (Sella et al., 2002) and the back-arc spreading rate of 0.035–0.050 m/year (Nishimura et al., 2004) along the Okinawa trough. This indicates that the main slip area is almost fully locked, and the accumulated strain due to plate convergence is mostly released by the SSEs.

5.2. Spatiotemporal Relationships Among SSEs, VLFEs, and LFEs

Along the southern Ryukyu subduction zone, seismic signals of slow earthquakes such as VLFEs and LFEs have been recently reported in addition to SSEs (Ando et al., 2012; Arai et al., 2016; Nakamura, 2017; Nakamura & Sunagawa, 2015). Figure 13 compares the cumulative slip distribution of SSEs from July 2010 to February 2013 with the epicenters of VLFEs (Nakamura & Sunagawa, 2015) and LFEs (Nakamura, 2017) during the same period, as well as the possible source area of the 1771 Yaeyama tsunami earthquake (Nakamura, 2009). Although the western limit of the slip area cannot be constrained due to the insufficient number of stations on Yonaguni Island, the SSEs mainly occur beneath Iriomote Island at depths of 30–60 km. Since several GNSS stations exist above the southern part of the main slip

area (see Figure 1), we consider that the upper limit of slip is largely resolved and this main slip area does not extend to shallower depths (<~30 km). On the other hand, VLFEs and LFEs are distributed complementarily with the SSEs, on the shallower part of the plate interface. Nakamura (2017) pointed out that LFEs form three large clusters on the south ends of Iriomote and Ishigaki Islands, while VLFEs are widely distributed due to the large uncertainties of their epicenters. Nakamura (2017) proposed that VLFEs and LFEs represent signals for different frequency bands of the same fault slip phenomena during the same period and concluded that most of VLFEs and LFEs occur in the same fault area, located along the shallow part of the plate boundary beneath the south end of the Yaeyama Islands (~15–25 km). Figure 13 indicates that the style of fault slip varies with depth along the southern Ryukyu subduction zone. There is a possible tsunamigenic zone in the shallowest part (~15 km), source regions of VLFEs and LFEs in the shallower part (~15–25 km), and the fault where SSEs occur in the deeper part (30–60 km), as also illustrated by Arai et al. (2016). This dependence of fault slips on depth can be interpreted as the changes with respect to depth of physical properties such as frictional properties and fluid pressure.

Our results indicate that the five SSEs in the southern Ryukyu area do not extend to the shallow (<~30 km) part of the plate interface (Figure 7). Furthermore, we do not find any SSEs shallower than the five detected SSEs. Dixon et al. (2014) and Rolandone et al. (2018) suggested that shallower SSEs may reduce the tsunami potential along the shallow part of the plate interface because those SSEs release at least part of the accumulated slip deficit and may limit coseismic rupture propagation. These previous studies, together with the absence of shallow slow slip found in this study, may be consistent with the possibility of shallow historical tsunami earthquake (Nakamura, 2009) and may imply future tsunami earthquakes in the southern Ryukyu subduction zone.

Daily numbers of VLFEs and LFEs show that swarm-like activities of VLFEs occur simultaneously with swarms of LFEs (Figure 8), although the number of detected LFEs is small due to a low signal-to-noise ratio. Nakamura and Sunagawa (2015) investigated the temporal relationships between SSEs and VLFEs along the plate interface in our study region. They obtained the daily occurrences of VLFEs averaged over 22 SSEs in our study area from 2002 to 2013 and concluded that VLFE activity often became 2 to 3 times greater than normal 10–20 days after the onset of SSEs. The present study indicates that VLFEs, and possibly LFEs, are activated in Event 3 (Figure 8c) 10–20 days after the initiation of the rapid acceleration of slip (Period II), although whether LFEs are activated or not is unclear due to the small event count. In contrast, there seems to be no obvious activation of VLFEs and LFEs during the other events. It is not clear why VLFEs and LFEs are activated during Event 3 but not during other events. One possible explanation is that stress accumulated in VLFE and LFE patches are heterogeneous before the onset of the SSEs. SSE occurrence results in a shear stress perturbation of ~1 kPa on the plate interface where VLFEs and LFEs occur (Nakamura & Sunagawa, 2015). If the accumulated stress in VLFE and LFE patches is high enough, the SSE stress perturbation would activate VLFEs and LFEs. Otherwise, activation of such events would not occur. This explanation is supported by the fact that tidal sensitivity of VLFEs is low in our study area because the shear stress change due to tides is comparable to that caused by SSEs (Nakamura & Kakazu, 2017). In summary, whether VLFEs and LFEs are activated or not might be dependent on the stress levels in VLFE and LFE patches at SSE onset time.

5.3. Implications for Physical Properties on the Fault

A wide variety of numerical and laboratory studies have shown that fault slip behavior during SSEs is determined by many physical factors such as frictional properties and stress state on the fault, geometry of the plate boundary, and, possibly, fluid pressure near the plate boundary. Previous studies have shown that frictional properties and effective normal stress on the fault control the depth extent, maximum slip rate, recurrence interval, and duration of SSEs (e.g., Leeman et al., 2016; Liu & Rice, 2007; Matsuzawa et al., 2013; Watkins et al., 2015). For example, Leeman et al. (2016) exhibited through laboratory experiments that the higher effective normal stress leads to lower maximum slip rate and longer duration. This indicates that temporal change of fluid distribution may explain the fundamental difference in temporal evolution of the SSEs in the southern Ryukyu area. These results suggest that detailed investigations of the spatiotemporal evolutions of SSEs may provide valuable information on such physical properties along the plate interface.

This study reveals that the cumulative slip distribution for the five SSEs along the southern Ryukyu Trench is quite similar among all events, while the spatiotemporal evolutions of slip, especially the nucleation style,

maximum slip rate, and duration, differ from event to event. Such variations in fault slip evolution during SSEs were also found in the Bungo channel (Ozawa et al., 2007; Yoshioka et al., 2015) and Boso areas (Fukuda, 2018) in Japan. Our results, together with the findings of these previous studies, suggest that some physical properties such as fluid pressure and frictional properties may change with time, or that the initial stress state on the plate interface immediately before the nucleation of the SSEs differs from event to event. Previous studies developed methods to quantitatively estimate physical properties along the plate interface including frictional properties, effective normal stress, and initial stress, based on transient postseismic geodetic signals or the geodetically derived spatiotemporal evolution of afterslip following large earthquakes (Fukuda et al., 2009; Kano et al., 2013, 2015). Application of these methods to the spatiotemporal evolution of slow slip obtained in this study may reveal whether the frictional properties and initial stress varies from event to event, leading to further understanding of the physical properties on the SSE fault and, ultimately, the generation mechanism of SSEs.

6. Conclusions

We investigate the spatiotemporal source processes of SSEs along the southern Ryukyu subduction zone in most southwestern part of Japan. The modified NIF is applied to GNSS time series from March 2010 to February 2013 and detects five SSEs with M_w ~6.6–6.7 and recurrence intervals of 5–9 months. Slip distributions of the five SSEs are quite similar, located beneath the northwestern coast of Iriomote Island at depths of 30–60 km. In contrast, the temporal evolutions of slip rate and moment rate vary with events. The most outstanding feature is that the nucleation style of SSEs is different from event to event; three of the five SSEs nucleate rapidly from zero to the maximum slip rate within several days, and the other two SSEs show a slow gradual nucleation lasting for 20–50 days. These SSEs repeatedly rupture the same fault area but evolve in different manners. The SSE source areas are complementarily located at the deeper part of VLFE and LFE source regions along the plate interface, and the SSE once activated the VLFEs and LFEs during our analysis period. The similarities and differences in the spatiotemporal evolutions of slip within the series of SSEs in the southern Ryukyu subduction zone, together with the relationships between the SSE evolution and VLFE/LFE activity, will help constrain the physical characteristics along the subduction interface and eventually elucidate SSE generation mechanisms.

Acknowledgments

We thank the two anonymous reviewers and the Editor for valuable comments to help improve the manuscript. The GNSS data were provided by the GSI and are available at the Japan Association of Surveyors. The GNSS data obtained by KU networks are available by contacting the corresponding author. We used the GIPSY-OASIS II software by the JPL. We thank T. Koike for formatting the GNSS data. VLFE and LFE catalogs used can be downloaded from *Slow Earthquake Database* (Kano et al., 2018; http://www-solid.eps.s.u-tokyo.ac.jp/~sloweq/), which is supported by JSPS KAKENHI JP16H06472. Generic Mapping Tools by Wessel and Smith (1998) are used to generate figures. This research was supported by the JSPS KAKENHI grant JP15K17743 in Grant-in-Aid for Young Scientists (B); JP18K03796 in Grant-in-Aid for Scientific Research (C); 21340127 in Grant-in-Aid for Scientific Research (B); JP16H06473 and JP16H06474 in Scientific Research on Innovative Areas *Science of Slow Earthquakes*; and the Ministry of Education, Culture, Sports, Science and Technology (MEXT) of Japan, under its Earthquake and Volcano Hazards Observation and Research Program.

References

Ando, M., Nakamura, M., Matsumoto, T., Furukawa, M., Tadokoro, K., & Furumoto, M. (2009). Is the Ryukyu subduction zone in Japan coupled or decoupled? The necessity of seafloor crustal deformation observation. *Earth, Planets and Space*, *61*, 1–9.

Ando, M., Tu, Y., Kumagai, H., Yamanaka, Y., & Lin, C.-H. (2012). Very low frequency earthquakes along the Ryukyu subduction zone. *Geophysical Research Letters*, *39*, L04303. https://doi.org/10.1029/2011GL050559

Arai, R., Takahashi, T., Kodaira, S., Kaiho, Y., Nakanishi, A., Fujie, G., et al. (2016). Structure of tsunamigenic plate boundary and low-frequency earthquakes in the southern Ryukyu trench. *Nature Communications*, *7*, 12255. https://doi.org/10.1038/ncomms12255

Bartlow, N. M., Miyazaki, S., Bradley, A. M., & Segall, P. (2011). Space-time correlation of slip and tremor during the 2009 Cascadia slow slip event. *Geophysical Research Letters*, *38*, L18309. https://doi.org/10.1029/2011GL048714

Bertiger, W., Desai, S. D., Haines, B., Harvey, N., Moore, A. W., Owen, S., & Weiss, J. P. (2010). Single receiver phase ambiguity resolution with GPS data. *Journal of Geodesy*, *84*(5), 327–337. https://doi.org/10.1007/s00190-010-0371-9

Boehm, J., Werl, B., & Schuh, H. (2006). Troposphere mapping functions for GPS and very long baseline interferometry from European Centre for Medium-Range Weather Forecasts operational analysis data. *Journal of Geophysical Research*, *111*, B02406. https://doi.org/10.1029/2005JB003629

Dixon, T. H., Jiang, Y., Malservisi, R., McCaffrey, R., Voss, N., Protti, M., & Gonzalez, V. (2014). Earthquake and tsunami forecasts: Relation of slow slip events to subsequent earthquake rupture. *Proceedings of the National Academy of Sciences*, *111*(48), 17,039–17,044. https://doi.org/10.1073/pnas.1412299111

Fukuda, J. (2018). Variability of the space-time evolution of slow slip events off the Boso Peninsula, central Japan, from 1996 to 2014. *Journal of Geophysical Research: Solid Earth*, *123*, 732–760. https://doi.org/10.1002/2017JB014709

Fukuda, J., Higuchi, T., Miyazaki, S., & Kato, T. (2004). A new approach to time-dependent inversion of geodetic data using a Monte Carlo mixture Kalman filter. *Geophysical Journal International*, *159*(1), 17–39. https://doi.org/10.1111/j.1365-246X.2004.02383.x

Fukuda, J., Johnson, K. M., Larson, K. M., & Miyazaki, S. (2009). Fault friction parameters inferred from the early stages of afterslip following the 2003 Tokachi-oki earthquake. *Journal of Geophysical Research*, *114*, B04412. https://doi.org/10.1029/2008JB006166

Fukuda, J., Kato, A., Obara, K., Miura, S., & Kato, T. (2014). Imaging of the early acceleration phase of the 2013-2014 Boso slow slip event. *Geophysical Research Letters*, *41*, 7493–7500. https://doi.org/10.1002/2014GL061550

Fukuda, J., Miyazaki, S., Higuchi, T., & Kato, T. (2008). Geodetic inversion for space-time distribution of fault slip with time-varying smoothing regularization. *Geophysical Journal International*, *173*(1), 25–48. https://doi.org/10.1111/j.1365-246X.2007.03722.x

Goto, K., Miyagi, K., Kawamata, H., & Imamura, F. (2010). Discrimination of boulders deposited by tsunamis and storm waves at Ishigaki Island, Japan. *Marine Geology*, *269*(1-2), 34–45. https://doi.org/10.1016/j.margeo.2009.12.004

Graham, S., DeMets, C., Cabral-Cano, E., Kostoglodov, V., Rousset, B., Walpersdorf, A., et al. (2016). Slow slip history for the Mexico subduction zone: 2005 through 2011. *Pure and Applied Geophysics*, *173*(10-11), 3445–3465. https://doi.org/10.1007/s00024-015-1211-x

Graham, S. E., DeMets, C., Cabral-Cano, E., Kostoglodov, V., Walpersdorf, A., Cotte, N., et al. (2014). GPS constraints on the 2011–2012 Oaxaca slow slip event that preceded the 2012 March 20 Ometepec earthquake, southern Mexico. *Geophysical Journal International*, *197*(3), 1593–1607. https://doi.org/10.1093/gji/ggu019

Hayes, G. P., Wald, D. J., & Johnson, R. L. (2012). Slab 1.0: A three-dimensional model of global subduction zone geometries. *Journal of Geophysical Research*, *117*, B01302. https://doi.org/10.1029/2011JB008524

Heki, K., & Kataoka, T. (2008). On the biannually repeating slow slip events at the Ryukyu trench, southwestern Japan. *Journal of Geophysical Research*, *113*, B11402. https://doi.org/10.1029/2008JB005739

Hirose, H., Matsuzawa, T., Kimura, T., & Kimura, H. (2014). The Boso slow slip events in 2007 and 2011 as a driving process for the accompanying earthquake swarm. *Geophysical Research Letters*, *41*, 2778–2785. https://doi.org/10.1002/2014GL059791

Hirose, H., & Obara, K. (2005). Repeating short- and long-term slow slip events with deep tremor activity around the Bungo channel region, south-west Japan. *Earth, Planets and Space*, *57*(10), 961–972. https://doi.org/10.1186/BF03351875

Hirose, H., & Obara, K. (2010). Recurrence behavior of short-term slow slip and correlated nonvolcanic tremor episodes in western Shikoku, southwest Japan. *Journal of Geophysical Research*, *115*, B00A21. https://doi.org/10.1029/2008JB006050

Ide, S., Beroza, G. C., Shelly, D. R., & Uchide, T. (2007). A scaling law for slow earthquakes. *Nature*, *447*(7140), 76–79. https://doi.org/10.1038/nature05780

Ito, Y., Hino, R., Kido, M., Fujimoto, H., Osada, Y., Inazu, D., et al. (2013). Episodic slow slip events in the Japan subduction zone before the 2011 Tohoku-Oki earthquake. *Tectonophysics*, *600*, 14–26. https://doi.org/10.1016/j.tecto.2012.08.022

Kano, M., Aso, N., Matsuzawa, T., Ide, S., Annoura, S., Arai, R., et al. (2018). Development of a slow earthquake database. *Seismological Research Letters*, *89*(4), 1566–1575. https://doi.org/10.1785/0220180021

Kano, M., Miyazaki, S., Ishikawa, Y., Hiyoshi, Y., Ito, K., & Hirahara, K. (2015). Real data assimilation for optimization of frictional parameters and prediction of afterslip in the 2003 Tokachi-oki earthquake inferred from slip velocity by an adjoint method. *Geophysical Journal International*, *203*(1), 646–663. https://doi.org/10.1093/gji/ggv289

Kano, M., Miyazaki, S., Ito, K., & Hirahara, K. (2013). An adjoint data assimilation method for optimizing frictional parameters on the afterslip area. *Earth, Planets and Space*, *65*(12), 1575–1580. https://doi.org/10.5047/eps.2013.08.002

Langbein, J., & Johnson, H. (1997). Correlated errors in geodetic time series: Implications for time-dependent deformation. *Journal of Geophysical Research*, *102*(B1), 591–603. https://doi.org/10.1029/96JB02945

Leeman, J. R., Saffer, D. M., Scuderi, M. M., & Marone, C. (2016). Laboratory observations of slow earthquakes and the spectrum of tectonic fault slip modes. *Nature Communications*, *7*, 1–6. https://doi.org/10.1038/ncomms11104

Liu, Y., & Rice, J. R. (2007). Spontaneous and triggered aseismic deformation transients in a subduction fault model. *Journal of Geophysical Research*, *112*, B09404. https://doi.org/10.1029/2007JB004930

Lyard, F., Lefevre, F., Letellier, T., & Francis, O. (2006). Modeling the global ocean tides: A modern insight from FES2004. *Ocean Dynamics*, *56*(5-6), 394–415. https://doi.org/10.1007/s10236-006-0086-x

Mao, A., Harrison, C. G. A., & Dixon, T. H. (1999). Noise in GPS coordinate time series. *Journal of Geophysical Research*, *104*(B2), 2797–2816. https://doi.org/10.1029/1998JB900033

Matsuzawa, T., Hirose, H., Shibazaki, B., & Obara, K. (2010). Modeling short- and long-term slow slip events in the seismic cycles of large subduction earthquakes. *Journal of Geophysical Research*, *115*, B12301. https://doi.org/10.1029/2010JB007566

Matsuzawa, T., Shibazaki, B., & Hirose, H. (2013). Comprehensive model of short- and long-term slow slip events in the Shikoku region of Japan, incorporating a realistic plate configuration. *Geophysical Research Letters*, *40*, 5125–5130. https://doi.org/10.1002/grl.51006

McGuire, J. J., & Segal, P. (2003). Imaging of aseismic fault slip transients recorded by dense geodetic networks. *Geophysical Journal International*, *155*(3), 778–788. https://doi.org/10.1111/j.1365-246X.2003.02022.x

Miyazaki, S., McGuire, J. J., & Segal, P. (2003). A transient subduction zone slip episode in southwest Japan observed by the nationwide GPS array. *Journal of Geophysical Research*, *108*(B2), 2087. https://doi.org/10.1029/2001JB000456

Nakamura, M. (2009). Fault model of the 1771 Yaeyama earthquake along the Ryukyu trench estimated from the devastating tsunami. *Geophysical Research Letters*, *36*, L19307. https://doi.org/10.1029/2009GL039730

Nakamura, M. (2017). Distribution of low-frequency earthquakes accompanying the very low frequency earthquakes along the Ryukyu trench. *Earth, Planets and Space*, *69*(1), 49. https://doi.org/10.1186/s40623-017-0632-4

Nakamura, M., & Kakazu, K. (2017). Tidal sensitivity of shallow very low frequency earthquakes in the Ryukyu trench. *Journal of Geophysical Research: Solid Earth*, *122*, 1221–1238. https://doi.org/10.1002/2016JB013348

Nakamura, M., & Sunagawa, N. (2015). Activation of very low frequency earthquakes by slow slip events in the Ryukyu trench. *Geophysical Research Letters*, *42*, 1076–1082. https://doi.org/10.1002/2014GL062929

Nishimura, S., Hashimoto, M., & Ando, M. (2004). A rigid block rotation model for the GPS derived velocity field along the Ryukyu arc. *Physics of the Earth and Planetary Interiors*, *142*(3–4), 185–203. https://doi.org/10.1016/j.pepi.2003.12.014

Nishimura, T. (2014). Short-term slow slip events along the Ryukyu trench, southwestern Japan, observed by continuous GNSS. *Progress in Earth and Planetary Science*, *1*(1), 22. https://doi.org/10.1186/s40645-014-0022-5

Obara, K., & Kato, A. (2016). Connecting slow earthquakes to huge earthquakes. *Science*, *353*(6296), 253–257. https://doi.org/10.1126/science.aaf1512

Ohta, Y., Freymueller, J. T., Hreinsdóttir, S., & Suito, H. (2006). A large slow slip event and the depth of the seismogenic zone in the south central Alaska subduction zone. *Earth and Planetary Science Letters*, *247*(1–2), 108–116. https://doi.org/10.1016/j.epsl.2006.05.013

Ozawa, S., Suito, H., Imakiire, T., & Murakmi, M. (2007). Spatiotemporal evolution of aseismic interplate slip between 1996 and 1998 and between 2002 and 2004, in Bungo channel, southwest Japan. *Journal of Geophysical Research*, *112*, B05409. https://doi.org/10.1029/2006JB004643

Peng, Z., & Gomberg, J. (2010). An integrated perspective of the continuum between earthquakes and slow-slip phenomena. *Nature Geoscience*, *3*(9), 599–607. https://doi.org/10.1038/ngeo940

Rebischung, P., Griffiths, J., Ray, J., Schmid, R., Collilieux, X., & Garayt, B. (2012). IGS08: The IGS realization of ITRF2008. *GPS Solutions*, *16*(4), 483–494. https://doi.org/10.1007/s10291-011-0248-2

Rogers, G., & Dragert, H. (2003). Episodic tremor and slip on the Cascadia subduction zone: The chatter of silent slip. *Science*, *300*(5627), 1942–1943. https://doi.org/10.1126/science.1084783

Rolandone, F., Nocquet, J. M., Mothes, P. A., Jarrin, P., Vallée, M., Cubas, N., et al. (2018). Areas prone to slow slip events impede earthquake rupture propagation and promote afterslip. *Science Advances*, *4*(1), eaao6596.

Rousset, B., Campillo, M., Lasserre, C., Frank, W. B., Cotte, N., Walpersdorf, A., et al. (2017). A geodetic matched-filter search for slow slip with application to the Mexico subduction zone. *Journal of Geophysical Research: Solid Earth*, *122*, 10,498–10,514. https://doi.org/10.1002/2017JB014448

Schmidt, D. A., & Gao, H. (2010). Source parameters and time-dependent slip distributions of slow slip events on the Cascadia subduction zone from 1998 to 2008. *Journal of Geophysical Research*, *115*, B00A18. https://doi.org/10.1029/2008JB006045

Schwartz, S. Y., & Rokosky, J. M. (2007). Slow slip events and seismic tremor at circum-Pacific subduction zones. *Reviews of Geophysics*, *45*, RG3004. https://doi.org/10.1029/2006RG000208

Segall, P., Desmarais, E. K., Shelly, D. R., Miklius, A., & Cervelli, P. (2006). Earthquakes triggered by silent slip events on Kilauea volcano, Hawaii. *Nature*, *442*(7098), 71–74. https://doi.org/10.1038/nature04938

Segall, P., & Matthews, M. (1997). Time dependent inversion of geodetic data. *Journal of Geophysical Research*, *102*(B10), 22,391–22,409. https://doi.org/10.1029/97JB01795

Sekine, S., Hirose, H., & Obara, K. (2010). Along-strike variations in short-term slow slip events in the southwest Japan subduction zone. *Journal of Geophysical Research*, *115*, B00A27. https://doi.org/10.1029/2008JB006059

Sella, G. F., Dixon, T. H., & Mao, A. (2002). REVEL: A model for recent plate velocities from space geodesy. *Journal of Geophysical Research*, *107*(B4), 2081. https://doi.org/10.1029/2000JB000033

Sibuet, J.-C., Deffontaines, B., Hsu, S.-K., Thareau, N., Formal, J.-P. L., Liu, C.-S., & ACT party (1998). Okinawa trough backarc basin: Early tectonic and magmatic evolution. *Journal of Geophysical Research*, *103*, 30,245–30,267. https://doi.org/10.1029/98JB01823

Szeliga, W., Melbourne, T., Santillan, M., & Miller, M. (2008). GPS constraints on 34 slow slip events within the Cascadia subduction zone, 1997–2005. *Journal of Geophysical Research*, *113*, B04404. https://doi.org/10.1029/2007JB004948

Thomas, A. L. (1993). Poly3D: A three-dimensional, polygonal element, displacement discontinuity boundary element computer program with applications to fractures, faults, and cavities in the Earth's crust, MS thesis, Stanford Univ., Stanford, Calif.

Tu, Y., & Heki, K. (2017). Decadal modulation of repeating slow slip event activity in the southwestern Ryukyu arc possibly driven by rifting episodes at the Okinawa trough. *Geophysical Research Letters*, *44*, 9308–9313. https://doi.org/10.1002/2017GL074455

Voss, N. K., Malservisi, R., Dixon, T. H., & Protti, M. (2017). Slow slip events in the early part of the earthquake cycle. *Journal of Geophysical Research: Solid Earth*, *122*, 6773–6786. https://doi.org/10.1002/2016JB013741

Wallace, L. M., & Beavan, J. (2010). Diverse slow slip behavior at the Hikurangi subduction margin, New Zealand. *Journal of Geophysical Research*, *115*, B12402. https://doi.org/10.1029/2010JB007717

Watkins, W. D., Colella, H. V., Brudzinski, M. R., Richards-Dinger, K. B., & Dieterich, J. H. (2015). The role of effective normal stress, frictional properties, and convergence rates in characteristics of simulated slow slip events. *Geophysical Research Letters*, *42*, 1061–1067. https://doi.org/10.1002/2014GL062794

Wdowinski, S., Bock, Y., Zhang, J., Fang, P., & Genrich, J. (1997). Southern California permanent GPS geodetic array: Spatial filtering of daily positions for estimating coseismic and postseismic displacements induced by the 1992 Landers earthquake. *Journal of Geophysical Research*, *102*(B8), 18,057–18,070. https://doi.org/10.1029/97JB01378

Wech, A. G., & Bartlow, N. M. (2014). Slip rate and tremor genesis in Cascadia. *Geophysical Research Letters*, *41*, 392–398. https://doi.org/10.1002/2013GL058607

Wessel, P., & Smith, W. H. F. (1998). New, improved version of Generic Mapping Tools released. *Eos Transactions American Geophysical Union*, *79*, 579.

Yoshioka, S., Matsuoka, Y., & Ide, S. (2015). Spatiotemporal slip distributions of three long-term slow slip events beneath the Bungo Channel, southwest Japan, inferred from inversion analyses of GPS data. *Geophysical Journal International*, *201*(3), 1437–1455. https://doi.org/10.1093/gji/ggv022

Zumberge, J. F., Heflin, M. B., Jefferson, D. C., Watkins, M. M., & Webb, F. H. (1997). Precise point positioning for the efficient and robust analysis of GPS data from large networks. *Journal of Geophysical Research*, *102*(B3), 5005–5017. https://doi.org/10.1029/96JB03860